Cytometry
PART A
Journal of the International Society for Advancement of Cytometry

Comparative Evaluation of Autofocus Algorithms for a Real-Time System for Automatic Detection of *Mycobacterium tuberculosis*

José María Mateos-Pérez,[1] * Rafael Redondo,[2] Rodrigo Nava,[3] Juan C. Valdiviezo,[4] Gabriel Cristóbal,[2] Boris Escalante-Ramírez,[5] María Jesús Ruiz-Serrano,[6] Javier Pascau,[7,8] Manuel Desco[7,8]

[1]CIBERSAM, Madrid, Spain

[2]Instituto de Óptica, CSIC, Spain

[3]Posgrado en Ciencia e Ingeniería de la Computación, Universidad Nacional Autónoma de México, Mexico City, México

[4]Instituto Nacional de Astrofísica, Óptica y Electrónica (INAOE), Tonantzintla, Puebla, México

[5]Facultad de Ingeniería, Universidad Nacional Autónoma de México, México City, México

[6]Servicio de Microbiología Clínica y Enfermedades Infecciosas, Hospital General Universitario Gregorio Marañón, Madrid, Spain

[7]Unidad de Medicina y Cirugía Experimental, Hospital General Universitario Gregorio Marañón, Madrid, Spain

[8]Departamento de Bioingeniería e Ingeniería Aeroespacial, Universidad Carlos III, Madrid, Spain

Received 27 September 2011; Revision Received 23 November 2011; Accepted 5 January 2012

Grant sponsor: UNAM (Universidad Nacional Autónoma de México); Grant number: PAPIIT IN113611; Grant number: IXTLI IX100610; Grant sponsor: Spanish Ministry of Science; Grant number: TEC2010-20307; Grant number: TEC2010-09834-E.

• Abstract

Microscopy images must be acquired at the optimal focal plane for the objects of interest in a scene. Although manual focusing is a standard task for a trained observer, automatic systems often fail to properly find the focal plane under different microscope imaging modalities such as bright field microscopy or phase contrast microscopy. This article assesses several autofocus algorithms applied in the study of fluorescence-labeled tuberculosis bacteria. The goal of this work was to find the optimal algorithm in order to build an automatic real-time system for diagnosing sputum smear samples, where both accuracy and computational time are important. We analyzed 13 focusing methods, ranging from well-known algorithms to the most recently proposed functions. We took into consideration criteria that are inherent to the autofocus function, such as accuracy, computational cost, and robustness to noise and to illumination changes. We also analyzed the additional benefit provided by preprocessing techniques based on morphological operators and image projection profiling.

• Key terms

autofocus; automatic diagnosis; fluorescence microscopy; top-hat filtering; tuberculosis

TUBERCULOSIS (TB) is an airborne infectious disease caused by the microorganism *Mycobacterium tuberculosis*. It is the main cause of death by any infectious disease today. In addition, it is endemic in developing countries and is considered an emerging disease in developed countries. According to the World Health Organization, a third of the world's population (1722 million people) carries this microorganism. A person can easily become infected with TB by inhaling tiny particles of infected sputum from the air. For this reason, early diagnosis may help in preventing transmission. The diagnosis can be made using indirect tests such as chest X-rays and the Mantoux test, or by direct observation of sputum smears. The latter technique can be used either with conventional microscopy (Ziehl-Neelsen stain) or with fluorescence microscopy (Auramine stain), which is more sensitive (1). Although the technique provides quick results, it requires highly trained personnel who may take up to 5 min per sample (2). Automation of the detection process could facilitate an early diagnosis, not only by saving time for specialists, but also by improving the sensitivity of detection as a consequence of exploring a potentially much higher number of fields.

Accurate focusing is critical in any automatic TB diagnostic system. Many autofocus algorithms have been proposed (3–7), although their accuracy depends to a large extent on the type of images being analyzed (3), and a universally valid solution for this particular problem does not exist. In particular, image features of

Additional Supporting Information may be found in the online version of this article.

*Correspondence to: José María Mateos-Pérez, Hospital Gregorio Marañón, Unidad de Medicina y Cirugía Experimental, Calle Doctor Esquerdo, 46, Madrid 28007, Spain.
Email: jmmateos@mce.hggm.es

Published online 30 January 2012 in Wiley Online Library (wileyonlinelibrary.com)

DOI: 10.1002/cyto.a.22020

fluorescence microscopy are very different from those of conventional or phase contrast microscopy. Furthermore, the possible usefulness of combining autofocus algorithms with preprocessing strategies such as median or morphological filtering has not been sufficiently validated. In this kind of images, the presence of debris in the samples may lead to focusing errors. Therefore, a preprocessing filtering stage may mitigate such effects, although the increase in computational cost of this stage has yet to be justified.

We assessed 13 autofocus algorithms used in sputum smear fluorescence images with the purpose of detecting TB bacilli using an automated setting: a motorized microscope attached to a computer that controls the focus. To require minimal changes to these settings, the computer also performs the functions of focus controller and image classifier. The assessment tries to account for the variability of these images in a real clinical environment (e.g. differences in luminosity depending on which sample region is being explored, time since staining, number of bacilli present, and artifacts). The variables evaluated are algorithm accuracy and computation time. We also analyzed how the algorithms performed when different preprocessing filters were applied and different levels of noise and nonhomogenous illumination were added.

Materials and Methods

Sample Preparation

The specimens were decontaminated using the *N*-acetyl-L-cysteine-sodium hydroxide procedure, and the sediment obtained was used for microscopy (Auramine smear) and culture on a solid slant (Löwenstein-Jensen Pyruvate) and a Mycobacterial Growth Indicator Tube (MGIT, Becton Dickinson). Smears were first air-dried and fixed using heat (100°C for 1 h). Auramine-O (1:1000 solution, in ethanol, phenol, and distilled water) was then flooded onto the slides to stain mycolic acid. After 15 min, the slides were washed with water and decolored using HCl (0.5% in ethanol). After 3–5 min, slides were again washed in water before being counterstained with thiazine red (0.5%) for 3 min. Slides were washed for the last time and air-dried.

Auramine smears were considered positive if at least three acid-fast bacilli were observed on the slide; the microscopist reviewed approximately 75–90 fields per slide before classing the smear as negative.

In cases of clinical suspicion, when the auramine smear was negative, *M. tuberculosis* was detected using the Amplified Mycobacterium Tuberculosis Direct test (Gen-Probe, bioMérieux).

Isolates of mycobacteria were identified by DNA probes (AccuProbe; Gen-Probe) for the *M. tuberculosis* complex strains, and an analysis of susceptibility to first line antituberculous drugs was performed using the Bactec MGIT 960 (Becton Dickinson) according to the manufacturer's procedures.

Hardware and Image Acquisition

A Nikon Eclipse 50i fluorescence microscope with a Nikon CFI Plan Fluor 20× lens (NA, 0.50; WD, 2.1 mm) was used. A ProScan motorized stage (Prior Scientific Instruments, Cambridge, United Kingdom) was attached to the microscope. The stage consisted of a mobile platform on the *XY* plane and a motorized control device adapted to the microscope focus knob (*Z*-axis) with a resolution of 0.1 μm per step (1 motor revolution equals 1000 steps). Images were acquired using a QImaging Retiga 2000R camera (QImaging, Surrey, Canada) with a resolution of 1600 × 1200 pixels. Exposure time was 0.25 s. The green channel of every image was stored as an 8-bit gray scale TIFF file. Since fluorescence information is more noticeable in the green channel than in any other, the red and blue channels were ruled out.

The software tools for controlling microscope XYZ movements and for implementing the autofocus functions were developed in Matlab 7.6.0 (The Mathworks, MA). The software was executed on an Intel Core2 QUAD 2.40 GHz 4 GB RAM computer using the Windows Vista operating system (Microsoft, WA).

Assessment of Focus Accuracy

Three hundred of 1037 stacks belonging to 10 different patients previously diagnosed at Hospital Universitario Gregorio Marañón were randomly chosen. Each stack consisted of 20-image stacks acquired at different focus points using a constant *Z* step ($\Delta z = 3$ μm) over the same field. The chosen step along the *Z*-axis was small enough for the visual difference between any two images around the focus point to be barely appreciable by a human observer. These 300 stacks are available for free for research purposes on the URL http://biig.uc3m.es/autofocus_stacks/.

Because of the small *Z*-axis step used, identification of the optimally focused image by human observers may not have a single solution, as different observers could choose slightly different images around the optimal focus plane. A single observer determined the optimal focus point used as the reference for the assessment of the automatic algorithms. To compare those algorithms with the human observer, a random sample of 30 stacks was focused by another four

observers and the overall standard deviation of the disagreement with the first observer was computed. This standard deviation was used as a threshold to assess whether a given algorithm focuses like a human being would do.

Autofocus functions were computed for each image of the stacks and total computation time was recorded. The maximum of the function for each algorithm was considered as the focus point, and the difference with the manually obtained focus point was considered the focus error. In addition, the percentage of correctly focused images, that is, those below the acceptance threshold, was computed.

For the five most accurate algorithms, the full width at half maximum (FWHM) and the peak-valley ratio for the function values were also computed. The function values were averaged in those stacks in which these five algorithms agreed at a given focus point.

Autofocus Algorithms

Thirteen different autofocus functions were used and evaluated:

- Vollath's F4 and F5 (VOL4, VOL5). This function is defined in (6):

$$F_{\mathrm{VOL4}} = \sum_{i=1}^{M-1}\sum_{j=1}^{N} g(i,j)\cdot g(i+1,j) - \sum_{i=1}^{M-2}\sum_{j=1}^{N} g(i,j)\cdot g(i+2,j) \tag{1.1}$$

  where $g(i, j)$ is the gray level of pixel g located at coordinates i, j and N and M are the image dimensions. This function computes the image autocorrelation and is reported as robust against noise and efficient in computational terms. A similar function is Vollath's F5 (7), which suppresses high frequencies:

$$F_{\mathrm{VOL5}} = \sum_{i=1}^{M-1}\sum_{j=1}^{N} g(i,j)\cdot g(i+1,j) - MN\bar{g}^{-2} \tag{1.2}$$

  where $\bar{g}$ is the mean pixel value in the image.
- *Log-histogram (LOG)*: Ref. (8) proposed a new method that made use of the brightness level of the image through a logarithmic transformation of the histogram. This measurement is based on the assumptions that the bacilli contribute solely to the upper part of the histogram, because they are brighter than background and other possible objects. This algorithm proposes the use of the image histogram modified by a logarithmic function as follows:

$$F_{\mathrm{LOG}} = \sum_{l}(l - E_{\log}(l))^2 \cdot \log(p_l) \tag{1.3}$$

  where

$$E_{\log}(l) = \sum_{l} l \cdot \log(p_l) \tag{1.4}$$

  where l is the gray level in the histogram (from 0 to 255) and p_l is the probability for each gray level.
- *Gaussian filter (GS)*: Ref. (3) published a function based on a gradient filter derived from the convolution of the image with a first-order Gaussian derivative.

$$F_{\mathrm{GS}} = \frac{1}{MN}\sum_{i,j}[g(i,j)\otimes G_i(i,j,\sigma)]^2 + [g(i,j)\otimes G_j(i,j,\sigma)]^2 \tag{1.5}$$

  To save processing time, it is possible to calculate its value in only one direction:

$$F_{\mathrm{GS}} = \frac{1}{MN}\sum_{i,j}[g(i,j)\otimes G_i(i,j,\sigma)]^2 \tag{1.6}$$

  In the previous equation, $G_i(i, j, \sigma)$ is the first-order Gaussian derivative with a scale of σ in the i direction. The value of σ depends on the elements of the image, and for bar-like structures this value should conform to $\sigma \approx \frac{d}{2}\sqrt{3}$, where d represents the thickness of the bar (the bacillus in this case), which should be chosen between 0.2 and 0.5 μm. The tested value for σ was 0.3 (GS03). Values of 1.0 (GS1) and 2.0 (GS2) were also tested to assess the behavior of this function with wider filters.
- *Energy of the image Laplacian (LAP)*: This focus measurement was originally used to find focusing errors caused by noise (5). It has desirable properties such as simplicity, rotational symmetry, and elimination of unnecessary information. The algorithm convolves a discrete Laplacian mask with the input image as follows:

$$F_{\mathrm{LAP}} = \sum_{i,j}[g(i-1,j) + g(i+1,j) + g(i,j-1) + g(i,j+1) - 4g(i,j)]^2 \tag{1.7}$$

- *Variance of the image (VAR)*: This focus measurement computes variations of pixel intensities and uses the power function to amplify larger differences from mean image intensity (4):

$$F_{\mathrm{VAR}} = \frac{1}{MN}\sum_{i,j}[g(i,j) - \bar{g}]^2 \tag{1.8}$$

  A modification of this same function involves a normalization step by using the mean brightness (NVAR):

$$F_{\mathrm{NVAR}} = \frac{1}{MN\bar{g}}\sum_{i,j}[g(i,j) - \bar{g}]^2 \tag{1.9}$$

- *Energy of the image (PS)*: This focus measure adds up all image intensities squared:

$$F_{\mathrm{PS}} = \sum_{i,j} g(i,j)^2 \tag{1.10}$$

- *Threshold (TH)*: This focus measure counts the number of pixels above a determined threshold, previously chosen according to the overall image brightness:

$$F_{\mathrm{TH}} = \sum_{i,j}(F(g(i,j))),\ F = \begin{cases} 1 \text{ if} & g(i,j) > \Theta \\ 0 & \text{otherwise} \end{cases} \tag{1.11}$$

The threshold Θ was set at 80% of the maximum brightness value in the whole stack.

- *Weighted histogram* (WHS). Focused images in fluorescence illumination exhibit a larger proportion of pixels with bright gray levels than unfocused images. Therefore, this procedure is based on a weighted image histogram without introducing a constant threshold (9). The procedure was performed empirically by multiplying the fifth root of the number of pixels of each gray level *h(i)* by the fifth power of this gray level *i* and dividing by 10^{15}. The sum of all transformed gray values was then used as a focus measurement.

$$F_{\mathrm{WHS}} = \sum_{l} 5\sqrt{h(l)} \cdot l^5 \cdot 10^{-15} \tag{1.12}$$

- *Hu's moments (HU)*: These moments, originally used as invariants, were recently used for the focus measure design in several ways (10). Here, we used a measurement based on a linear combination of second-order moments, as follows:

$$F_{\mathrm{HU}} = \mu_{20} + \mu_{02} = \sum_{i,j}(i - i_c)^2 \cdot g(i,j) + \sum_{i,j}(j - j_c)^2 \cdot g(i,j), \tag{1.13}$$

where $i_c = \frac{c_{10}}{c_{00}}$ and $j_c = \frac{c_{10}}{c_{00}}$ are, respectively, the horizontal and vertical centroids of the image, defined as:

$$c_{pq} = \sum_{i,j} i^p \cdot j^q \cdot g(i,j) \tag{1.14}$$

Hu's moments were computed using tiles of 20 × 10 pixels over each image of the stack. The results were averaged and used as the focus measurement. Although we present data for tiles measuring 20 × 10 pixels, other tile sizes offered similar results.

- *Tenengrad (TEN)*: This algorithm convolves an image with Sobel operators and sums the square of all the magnitudes greater than a threshold (11,12).

$$F_{\mathrm{TEN}} = \sum_{i,j}[g(i,j) \otimes S]^2 + [g(i,j) \otimes S']^2, \tag{1.15}$$

where S and S' are Sobel's kernel and its corresponding transpose, respectively:

$$S = \begin{bmatrix} 1 & 0 & -1 \\ 2 & 0 & -2 \\ 1 & 0 & -1 \end{bmatrix} \tag{1.16}$$

Although the original implementation of the Tenengrad algorithm uses a threshold, we decided to include all the pixels in the summation.

- *Absolute Tenengrad (ATEN)*: This focus measurement is similar to the previous one, but here the absolute value of the gradient coefficients is taken in order to reduce the computational cost. This technique is known as absolute gradient and was proposed in (13).

$$F_{\mathrm{ATEN}} = \sum_{i,j} |g(i,j) \otimes S| + |g(i,j) \otimes S'| \tag{1.17}$$

- *Discrete cosine transform (DCT)*: According to (14), focusing techniques based on band-pass filters perform well. In this algorithm, images are divided into blocks of 40 × 40 pixels, DCT is applied, and the sum of four band-pass diagonal bands representing mid and high frequencies is chosen (15):

$$c(p,q) = \frac{1}{16}\sum_{i,j} g(i,j)\cos\left(\frac{\pi(2m+1)p}{2M}\right)\cos\left(\frac{\pi(2n+1)q}{2N}\right) \tag{1.18}$$

- *Midfrequency-DCT (MDCT)*: The effect of the band-pass DCT coefficients on the focus measure has been analyzed by (16). The same authors proposed a 4 × 4 DCT operator to extract the central coefficient $c(4,4)$, which is used as a focus measurement. The MDCT operator can be calculated as:

$$F_{\mathrm{MDCT}} = \sum_{i,j}(g(i,j) \otimes O_{\mathrm{MDCT}})^2, \tag{1.19}$$

with

$$O_{\mathrm{MDCT}} = \begin{bmatrix} 1 & 1 & -1 & -1 \\ 1 & 1 & -1 & -1 \\ -1 & -1 & 1 & 1 \\ -1 & -1 & 1 & 1 \end{bmatrix} \tag{1.20}$$

- *Total variation (TV)*: This algorithm is essentially an L_1 norm of the image derivatives in both directions (17). Therefore,

$$F_{\mathrm{TV}} = \sum_{i,j} |g_x(i,j)| + |g_y(i,j)| \tag{1.21}$$

where g_x and g_y are the derivatives in the x and y directions of the image, respectively.

Filtering

The effect of different preprocessing techniques on the final result was tested by applying several filters, namely, 2 × 2, 4 × 4, and 8 × 8 median filters, as well as a morphological top-hat (18) algorithm using a 9 × 9 pixel square mask. The goal of the median filter is to reduce noise on the image. The top-hat filter is used to remove elements bigger than bacilli. This technique was previously assessed by (19), with good results, although in this study a larger number of autofocus functions are evaluated. This morphological operator performs a successive opening and closing operation with a squared (in our case) structural element which has the property of removing small objects and preserving bigger ones. The result is then subtracted from the original image, providing a final image with the bigger objects removed. As a side effect of this kind of filtering, the shape of small particles could be

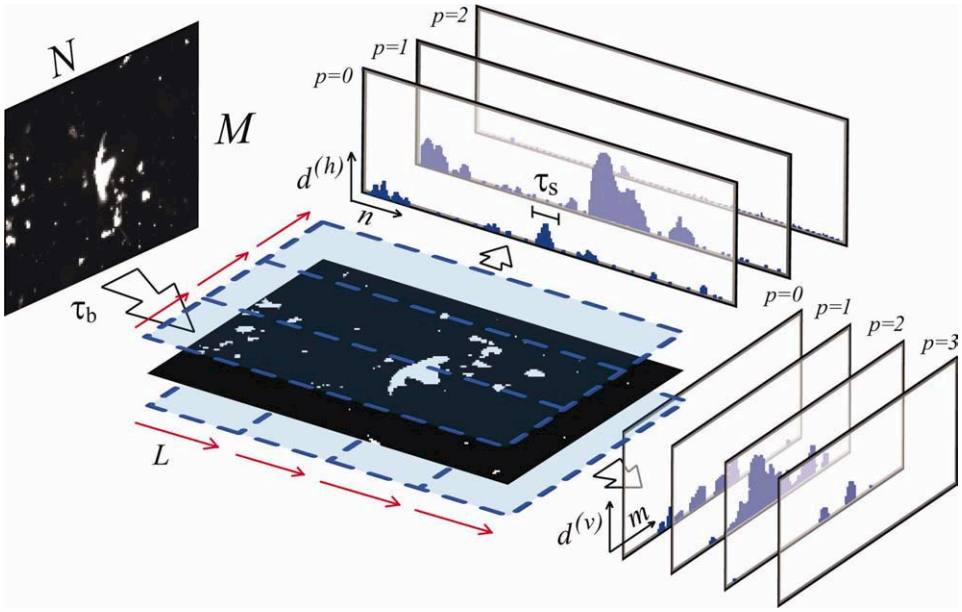

Figure 1. Schematic representation of the profiling method for estimating particle sizes. The image is binarized using the threshold τ_b and then divided into horizontal and vertical rectangular tiles. The size of the particles is estimated as the length of the contiguous projected values greater than zero. If at least one size is greater than a threshold τ_s, then the top-hat filter is applied. [Color figure can be viewed in the online issue, which is available at wileyonlinelibrary.com.]

modified. This effect is not relevant for the purpose of this study, since the desired result is merely the optimal focus point and the image is not further processed.

The median and top-hat filters were applied to the stored green-channel grayscale images, and the time used by each filtering method was recorded.

Profile Projection

Because top-hat filtering is computationally expensive, it should preferably be applied only to those image stacks with large objects. To determine whether it should be applied, we propose the application of a profile projection method that binarizes the image and projects the pixels in vertical and horizontal directions. The largest size of the particles is estimated as the length of the contiguous projected values that are greater than zero. However, size estimation could fail if the binarization process is inappropriate or if there is a high density of small particles. To reduce the likelihood of such a problem, the binarized image is projected in rectangular tiles in both horizontal and vertical directions. The projection of these profiles can be considered as a measure of blob density as follows:

$$d_p^{(h)}(n) = \sum_{i=1+p.L}^{(p+1).L} T_{\tau_b}[g(i,j)], p = \{0,1,\ldots\}$$
$$d_p^{(v)}(n) = \sum_{j=1+p.L}^{(p+1).L} T_{\tau_b}[g(i,j)], p = \{0,1,\ldots\} \quad (1.22)$$

where $d_p^{(h)}$ and $d_p^{(v)}$ are the p-th horizontal and vertical density of the binarized profiles and L is the shorter tile distance. Note that the aim here is not to calculate precisely the areas and widths of the particles, but to obtain an estimate of the particle size in order to decide whether or not top-hat filtering should be applied. Figure 1 shows a scheme of the profiling projection method. In this study, we used $L = 400$, (e.g. tiles measuring 400×600 pixels and 400×1200 pixels), a binarization threshold of $\tau_b = 100$, and a threshold that gears the application of the top-hat when at least one of the estimated sizes is greater than $\tau_s = 80$.

Noise

To assess the robustness of the autofocus functions against noise, they were evaluated again with the addition of Poisson noise to the original images with no filtering process. This addition was implemented using the Matlab *poissrnd* function with several λ values ($\lambda = 10$, 20, 45, and 90).

Nonhomogeneous Illumination

The behavior of the autofocus functions was also tested under conditions of nonhomogeneous illumination. This was simulated using a luminance gradient as a quadratic polynomial function represented as a gray-level image which multiplied the original images. Different maximum intensity values were used (0.8, 0.9, and 1.0); the minimum was always 0.

Results

The standard deviation of the focus position for the human observers was 3.60 μm. Therefore, the maximum error value above which the image is considered not properly focused (acceptance threshold) was set at 7.20 μm. That means a difference less or equal to 2 motor steps.

The errors for each autofocus function are shown in Figure 2a. When no prefiltering is used, several methods focus

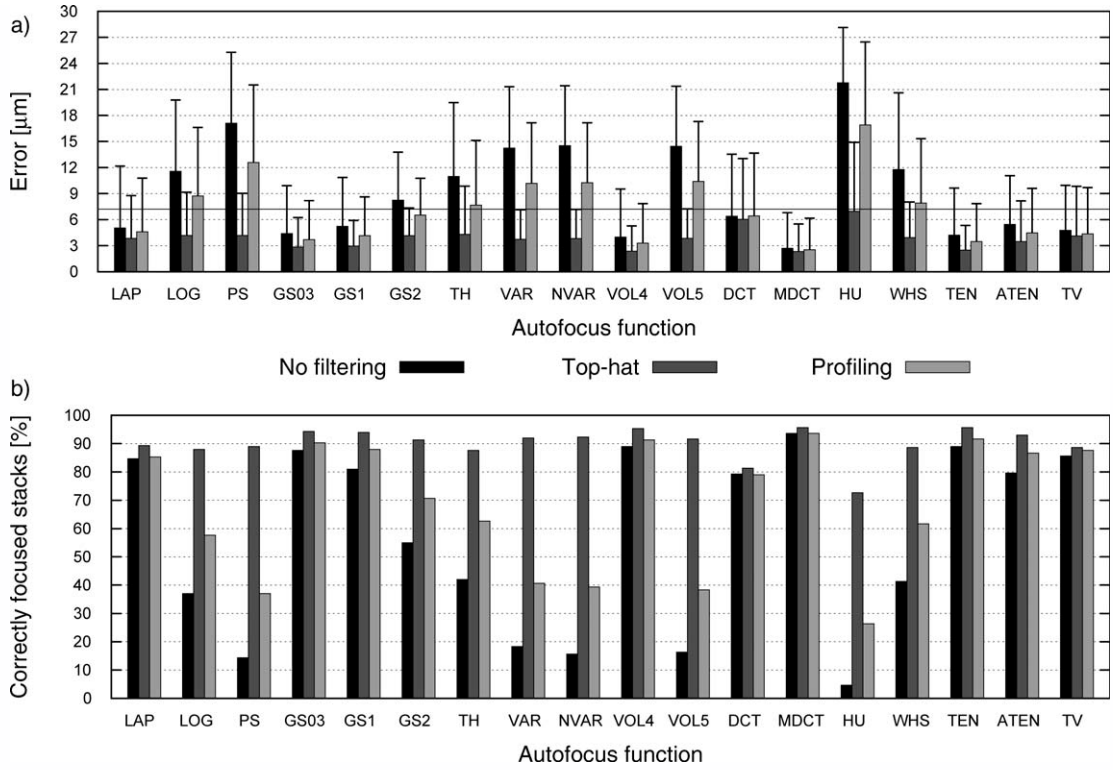

Figure 2. (**a**) Mean error for each algorithm and preprocessing method. The horizontal line marks the acceptance threshold used. (**b**) Percentage of images correctly focused. Please refer to the Supplementary Information for numerical data.

below the maximum allowed error: MDCT (error = 2.69 ± 4.11 μm), VOL4 (3.99 ± 5.55 μm), TEN (4.21 ± 5.42 μm), and GS03 (4.40 ± 5.50 μm).

The median filters did not improve the results for a mask size of 2 × 2. The results were worse in the case of mask sizes of 4 × 4 (7.98% of the samples fell outside the focus zone)

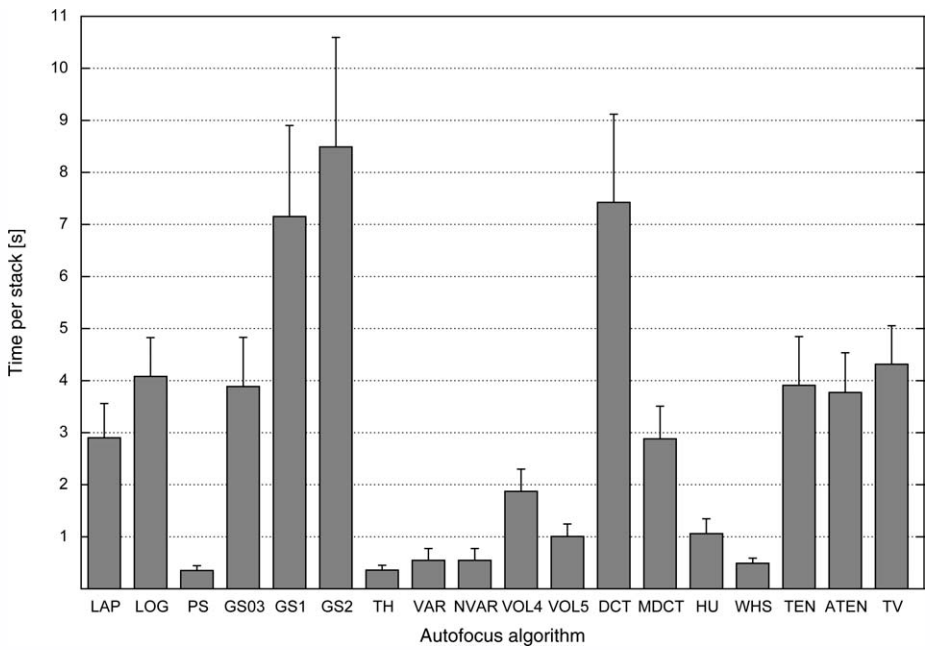

Figure 3. Mean time required by each autofocus algorithm per stack. Please refer to the Supplementary Information for numerical data.

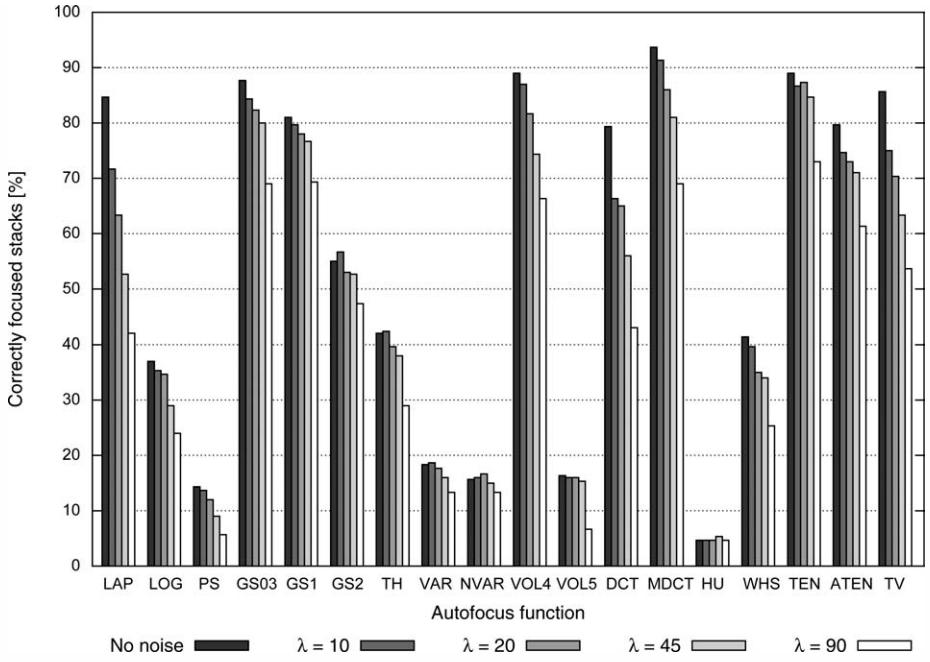

Figure 4. Percentage of correctly focused stacks when different levels of noise are added to the original images. Please refer to the Supplementary Information for numerical data.

and 8 × 8 (37.26% worsening). In any case, none of these filters noticeably improved the results. In addition, the improvement was small or nonexistent for the algorithms with the best performance. Therefore, these results are not included in this Figure 2.

When top-hat filtering was applied, all the autofocus functions reduced their error below the acceptance threshold, except for DCT (6.79 ± 7.92 μm) and HU (6.04 ± 7.00 μm).

In addition to the mean error, a more relevant metric is the percentage of correctly focused images (focused below the acceptance threshold). In Figure 2b, we can see that the most accurate algorithms were MDCT (96.67%), TEN (89%), VOL4 (89%), GS03 (86.67%), and TV (85.67%).

The computation times for each algorithm are shown in Figure 3. Top-hat filtering took 7.42 ± 1.29 s per stack, and the profile projection technique took 6.48 ± 3.97 s per stack.

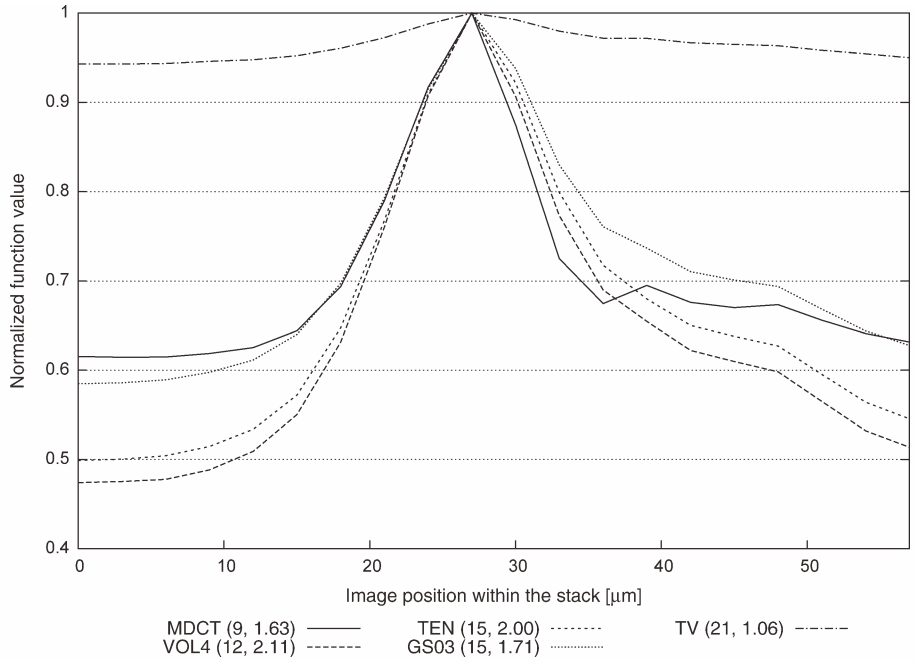

Figure 5. Normalized values for the average value of the five most accurate autofocus functions. The numbers in parenthesis represent the FWHM in μm and the peak-valley ratio.

No differences were found in the computation time required by the different autofocus functions depending on whether prefiltering was applied or not.

The results for each algorithm with different levels of noise present in the images can be seen in Figure 4.

No differences in algorithm performance were detected when nonhomogenous illumination was simulated. Most showed a slight decrease in accuracy (<5%), independently of the maximum illumination gradient used. Accuracy was slightly increased for four algorithms: LOG (7.33% increase), PS (3%), NVAR (4%), and WHS (14%). This increment was not independent of the maximum gradient; the values shown here belong to the maximum improvement achieved for a gradient of 0.8.

The results of the FWHM and peak-valley ratio study are shown in Figure 5 for MDCT, VOL4, TEN, GS03, and TV. The normalized function values were calculated by averaging 30 stacks in which all the functions agreed on the same focus point (located 27 μm from the beginning of the stack).

The characteristic effects of top-hat filtering on an image can be seen in Figure 6. The effects of the different types of filtering on the function values can be seen in Figure 7 (VOL4 sample).

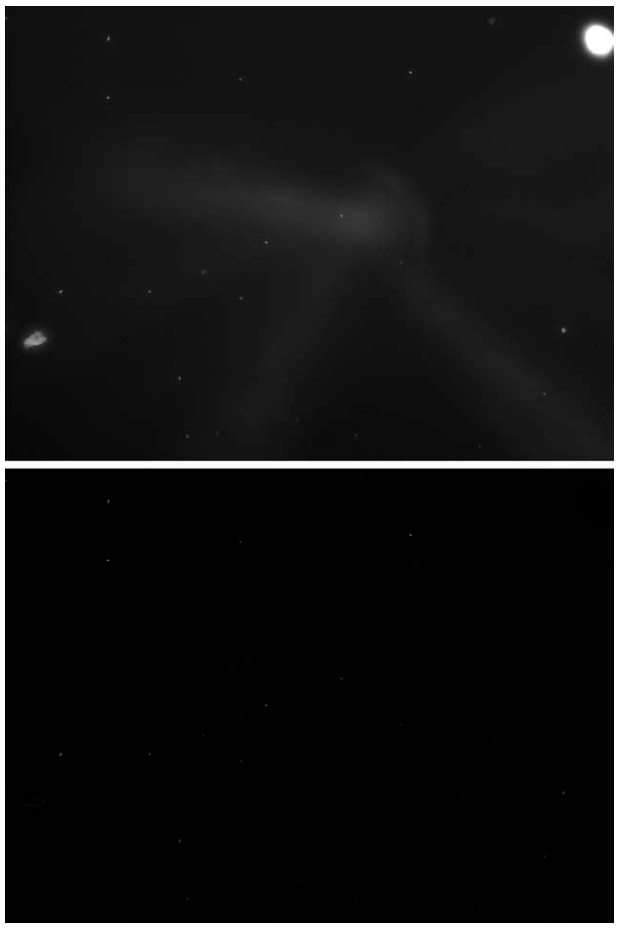

Figure 6. Effects of top-hat filtering. The original image (top) presents large elements that are removed (bottom) when top-hat filtering is used.

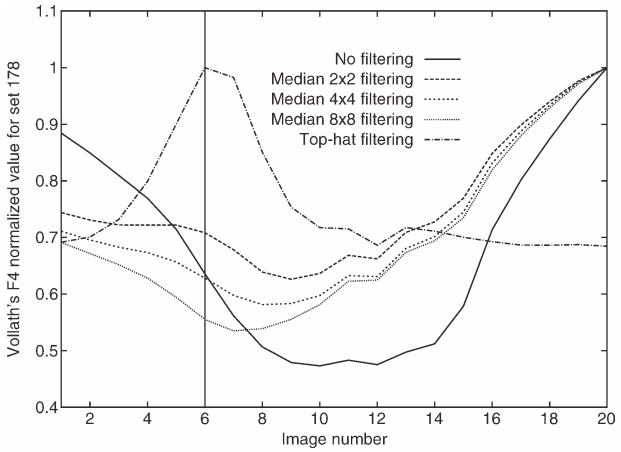

Figure 7. Effects of top-hat filtering on the normalized values for VOL4 for the same stack used in Figure 6. The vertical line marks the focused image.

Discussion

Accurate focusing is vital for correct identification of objects under the microscope and, consequently, for an automated diagnostic system. Many previous works compare the efficiency of different autofocus algorithms. In this study, we took into account several aspects that are relevant for a real-time application: variability of the fluorescent microscopy images, addition of noise, illumination changes, and prefiltering processes. The final goal of this study was to assess the appropriateness and robustness of a series of focusing algorithms and preprocessing techniques to select one for a future automatic diagnostic application. Although more autofocus algorithms could have been included, the current selection offers a good balance between old and new techniques that are most commonly used.

With our data, VOL4, MDCT, and TEN achieved the best results with non-prefiltered images. When all the evaluated algorithms were ordered by accuracy, the resulting ranking was consistent with those of previous reports (5,6,20), considering that not all of them evaluated the same functions.

The median filter was included in our tests because it is a fast and reliable algorithm for removing noise without impairing resolution. Our data showed it to have almost no effect on the accuracy of the tested algorithms when the mask is small and a negative effect (loss of accuracy) when the mask size increased to 8 $\times$ 8 pixels. Therefore, its use is discouraged for the type of images we work with.

Another type of filter that has proven successful is the morphological top-hat filter, which, in our case, was used to eliminate large objects from the image and leave only the smaller bacilli (Fig. 6). This filter increased the accuracy of all the algorithms assessed. The explanation for the poor accuracy of several focusing functions is the presence of large elements that are not the desired focus target; only those algorithms

that are more sensitive to small elements performed better. Once the top-hat filter eliminated the large structures, the performance of the focusing functions improved. An example of the evolution of the function shape depending on the filtering method used can be seen in Figure 7 for VOL4. However, the high computational cost of this filter makes it unfeasible in a true real-time detection system. To overcome this drawback, we propose a new method for estimating particle size in the image, based on projection profiling of binarized and tiled images, which helps to reduce the computational cost by about 19% with low error impairment (Fig. 2). This reduction is not effective enough for a real-time system, so the use of field programmable gate arrays or graphics processing units could be considered in the future to increase overall speed. In any case, the improvement in computational cost may not be substantial enough to justify its implementation if a fast, hardware-based solution is available.

Robustness of the focusing algorithms regarding noise is important when working in low signal-to-noise conditions, such as poor illumination or reduced acquisition times. To evaluate performance under such situations, we tested the effect of adding Poisson noise and nonhomogeneous illumination. When the noise level is low ($\lambda \leq 20$), TEN, along with GS03, is the most robust algorithm—in terms of noise—of all those with good results. When using higher noise levels, the accuracy of all the algorithms is severely affected.

In the presence of nonhomogeneous illumination, the results did not change noticeably. This supports the idea that the tested algorithms are quite robust and independent of the light source. The LOG, PS, and WHS algorithms actually increased their accuracy when the illumination was nonhomogeneous; however, considering that their accuracy under normal conditions is very low, this particular result lacks relevance. In the case of LOG and WHS, which are the two functions that showed the largest increase in accuracy, the results did not change, probably because of the modification of the histogram, given that both these methods use it to compute their value for each image.

The objective of this study was to progress to an easy and rapid automatic focusing system for an entire sample, for instance, by defining efficient whole-slide scanning strategies (e.g. using a coarse to fine search procedure or other optimal searching method such as the Fibonacci search). To accomplish this, it is important to notice that even when several functions showed similar degrees of accuracy, some of them displayed FWHM and the peak-valley ratios that make them more suitable for an optimization process, as seen in Figure 5. In this study, VOL4 and TEN presented a higher ratio, and MDCT and VOL4 were the functions that more rapidly converged to the focus point. TV, on the other hand, is a slow function, and the maximum and the minimum values are close.

Conclusions

Several autofocus algorithms were assessed under different conditions of illumination and noise in fluorescence-labeled *Mycobacterium tuberculosis* samples. For those applications where the computing time is important, we recommend the use of MDCT or VOL4, as they showed the best accuracy and had a low computational cost. Median prefiltering did not improve the results. Small-object selection by top-hat morphological preprocessing increased accuracy, although at a computational cost that is not affordable for a real-time application.

Acknowledgments

We thank Juan Aguirre for his valuable suggestions. Juan C. Valdiviezo thanks the National Council of Science and Technology (CONACYT) for doctoral scholarship No. 175027.

Literature Cited

1. Steingart KR, Henry M, Ng V, Hopewell PC, Ramsay A, Cunningham J, Urbanczik R, Perkins M, Aziz MA, Pai M. Fluorescence versus conventional sputum smear microscopy for tuberculosis: A systematic review. Lancet Infectious Diseases 2006;6:570–581.
2. International Union Against Tuberculosis and Lung Disease (IUATLD) technical guide: Sputum examination for tuberculosis by direct microscopy in low-income countries. Paris: International Union Against Tuberculosis and Lung Disease; 2000.
3. Geusebroek JM, Cornelissen F, Smeulders AW, Geerts H. Robust autofocusing in microscopy. Cytometry 2000;39:1–9.
4. Groen FC, Young IT, Ligthart G. A comparison of different focus functions for use in autofocus algorithms. Cytometry 1985;6:81–91.
5. Russell MJ, Douglas TS. Evaluation of autofocus algorithms for tuberculosis microscopy. Conference proceedings: Annual International Conference of the IEEE Engineering in Medicine and Biology Society 2007:3489–3492.
6. Santos A, Ortiz De Solórzano C, Vaquero JJ, Peña JM, Malpica N, del Pozo F. Evaluation of autofocus functions in molecular cytogenetic analysis. J Microsc 1997;188:264–272.
7. Vollath D. The influence of the scene parameters and of noise on the behaviour of automatic focusing algorithms. J Microsc 1988;151:133–146.
8. Forero M, Sroubek F, Cristobal G. Identification of tuberculosis bacteria based on shape and color. Real-Time Imag 2004;10:251–262.
9. Zeder M, Pernthaler J. Multispot live-image autofocusing for high-throughput microscopy of fluorescently stained bacteria. Cytometry Part A 2009;75A:781–788.
10. Flusser J, Suk T, Zitova B. Moments and Moments Invariant in Pattern Recognition. UK: Wiley; 2009.
11. Krotkov E. Focusing. Int J Comput Vision 1988;1:223–237.
12. Schlag JF, Sanderson AC, Neuman CP, Wimberly FC. Implementation of automatic focusing algorithms for a computer vision system with camera control. Tech report CMU-RI-TR-83-14, Robotics Institute, Carnegie Mellon University, August, 1983 (http://www.ri.cmu.edu/publication_view.html?pub_id=61).
13. Jarvis RA. Focus optimization criteria for computer image processing. Microscope 1976;24(2):163–180.
14. Subbarao M, Choi T, Nikzad A. Focusing techniques. J Opt Eng 1992;32:2824–2836.
15. Charfi M, Nyeck A, Tosser A. Focusing criterion. Electron Lett 1991;27:1233–1235.
16. Lee S-Y, Kumar Y, Cho J-M, Lee S-W, Kim S-W. Enhanced autofocus algorithm using robust focus measure and fuzzy reasoning. IEEE Trans Circuits Syst Video Technol 2008;18:1237–1246.
17. Rudin LI, Osher S, Fatemi E. Nonlinear total variation based noise removal algorithms. Physica D Nonlinear Phenomena 1992;60:259–268.
18. Vincent L. Morphological area openings and closings for grey-scale images. Proceedings of the NATO Shape in Picture Workshop. Driebergen, The Netherlands: Springer; 1992. pp 197–208.
19. Hilsenstein V. Robust autofocusing for automated microscopy imaging of fluorescently labelled bacteria. DICTA ' 05. Proceedings Digital Image Computing: Technqiues and Applications, 2005. pp 95–101.
20. Osibote OA, Dendere R, Krishnan S, Douglas TS. Automated focusing in bright-field microscopy for tuberculosis detection. J Microsc 2010;240:155–163.